



Numerical simulation of bubble rising in viscous liquid

Jinsong Hua^{*}, Jing Lou

Institute of High Performance Computing, 1 Science Park Road, #01–01, The Capricorn, Singapore Science Park II, Singapore 117528, Singapore

Received 27 February 2006; received in revised form 19 July 2006; accepted 20 August 2006
Available online 2 October 2006

Abstract

An improved numerical algorithm for front tracking method is developed to simulate the rising of a bubble in quiescent viscous liquid due to buoyancy. In the new numerical algorithm, volume correction is introduced to conserve the bubble volume while tracking the bubble's rising and deforming, and volume flux conservation based SIMPLE algorithm is adopted to solve the Navier–Stokes equation for fluid flow using finite volume method. The new front tracking algorithm is validated systematically by simulating single bubble rising and deforming in quiescent viscous liquid under different flow regimes. The simulation results are compared with the experimental measurement in terms of terminal bubble shape and velocity. The simulation results demonstrate that the new algorithm is robust in the flow regimes with larger ranges of Reynolds number ($Re < 200$), Bond number ($Bo < 200$), density ratio ($\rho_l/\rho_b < 1000$) and viscosity ratio ($\mu_l/\mu_b < 500$). The new front tracking algorithm is also applied to investigate bubble rising and deforming behaviour in the various flow regimes of “air bubble/water solution” system under effects of Reynolds number, Bond number, density ratio, viscosity ratio as well as the bubble initial shape, which have been explored previously by experiments. The predicted bubble shape and terminal velocity agree well with the experimental results. Hence, the new modelling algorithm expands the conventional front tracking method to more realistic and wider applications.

© 2006 Elsevier Inc. All rights reserved.

Keywords: Front tracking method; Incompressible flow; SIMPLE algorithm; Bubble rising; Two-phase flow; Computational fluid dynamics

1. Introduction

Multi-fluid systems play an important role in many natural and industrial processes such as combustion/chemical reaction, petroleum refining and boiling. The rising of single bubble in a viscous liquid due to buoyancy is one of typical multi-fluid systems. A fundamental understanding of the bubble rising physics is essential in various practical applications, ranging from the rise of steam bubble in boiler tubes to gas bubbles in oil well. However, a comprehensive knowledge of the flow behaviour and mechanism of such multi-fluid systems

^{*} Corresponding author.

E-mail address: huajs@ihpc.a-star.edu.sg (J. Hua).

in full flow regimes is still lacking, although a number of experimental, theoretical analysis and numerical studies have addressed this problem.

Early studies on the rise of a bubble in an inviscid or a viscous fluid were reported in the works of Hartunian and Sears [11], Walters and Davidson [28,29], Wegener and Parlange [30], and Bhaga and Weber [1]. However, our understanding on bubble rise and deformation is still limited to a few flow regimes only, due to the difficulties in experiments. It is rather difficult to measure, without any interference, the flow pattern and pressure distribution within a bubble and its surrounding liquid while it is rising and deforming. As a result, approximate theoretical solutions have been derived in the limit of very small bubble deformations (low Bond number) for either high [16] or low [26] Reynolds numbers, where the bubble shape is relatively stable. In the analysis work of Davies and Taylor [8], the rising speed of a spherical-cap bubble was related to the radius/curvature of the bubble at the forward stagnation point. Hence, they took the overall spherical-cap as a priori shape rather than being determined as part of solution. Considering the difficulties in experimental and theoretical investigations, numerical simulations provide an effective alternative approach to attain a better insight into the bubble rising behaviour, the development of bubble shape evolution and the flow behaviour in the viscous liquid.

Correct simulation of the flow behaviour in a multi-fluid system depends upon the ability of numerical model to satisfactorily characterise the flow mechanism for each fluid phase as well as the interactions between them. In recent years, significant progress has been made in understanding and modelling complex single-phase flows by advanced flow visualisation technique, detail flow field measurements and sophisticated numerical simulations. In principle, the multi-fluid systems could also be numerically modelled using the same governing-equations (Navier–Stokes equations and mass conservation equation) for single-phase flow. However, the sharp interface in multi-fluid system may lead to discontinuities of fluid properties such as density and viscosity in the flow field. In addition, the existence of surface tension would induce a pressure jump across the interface as well. Hence, some numerical schemes for single-phase flow simulation cannot be directly extended for multiphase flows. All these facts present difficulties in the numerical modelling of the multi-fluid systems. If the numerical method is of lower order accuracy, excessive numerical diffusion will smear the sharpness of the front. On the other hand, a higher order scheme may lead to numerical oscillations near the front that may propagate further to other parts in the solution domain. To overcome these obstacles in tracking the sharp interface for the multi-phase flows, various numerical methods, such as VOF method [12], level set method [18], front tracking method [6,7,9,10,27] and surface fitted method [2,13,23] have been proposed. Detail reviews on these numerical methods have been reported in the works of Van Sint Annaland and Kuipers [25] and Scardovelli and Zaleski [24].

In the present work, the state of art front tracking method, a hybrid approach of the front capturing and tracking technique proposed by Tryggvason et al. [27], was examined. In this method, a stationary, fixed grid is used for the fluid flow, and a set of adaptive elements is used to mark the interface. One set of Navier–Stokes equations is solved in the whole computational domain by treating the different phases as one fluid with variable material properties. The fluid properties such as density and viscosity are calculated according to the position of the interface. Hence, this method could avoid numerical diffusion, and capture sharp interfaces. Interfacial source terms such as surface tension are computed on the front and then transferred to the fixed grid using a δ (dirac-delta) function on the interface between the phases. The position of the interface is advected explicitly using the velocity interpolated from the flow field on the background grid.

The front tracking method has been applied to solve various interfacial flow problems [27]. It has been reported by Bunner and Tryggvason [3] that the capability of conventional algorithm is limited to lower density ratios, lower Reynolds numbers and lower Bond numbers. A further extension of this method is proposed in the present work to make it applicable to wider flow regimes. In the traditional approach, the governing Navier–Stokes equation is discretized using finite-difference scheme and solved using projection method. In the present paper, the unsteady Navier–Stokes equation is discretized by the conventional finite volume method and solved numerically using a modified SIMPLE method [19]. The interface is tracked explicitly with the advection velocity that is interpolated from the fixed background grid. The front mesh size is adapted through coarsening and refining, when the front moves and the front mesh is distorted. Because of the explicit front tracking approach and front mesh adaptation the conservation of the volume inside the front is not

guaranteed. Hence, a volume correction scheme is applied in this paper to conserve the volume enclosed inside the front mesh.

As a benchmarking test, the improved algorithm is used to model single air bubble rising in viscous liquid, which has been treated widely as typical cases to validate numerical methods for interfacial flows in the past works of Raymond and Rosant [22], Chen et al. [4] and Ohta et al. [17]. However, most of previous simulations are performed under conditions of lower density ratio, the simulation results are just validated against experimental observations about bubble shape under some typical flow regimes only [4,17]. There are only few quantitative comparisons about bubble terminal velocity, e.g. in the work of Koebe et al. [14]. In this paper, the improved front tracking method is used to systematically investigate single air bubble rising in water solutions within wider flow regimes. The simulation results are compared with experimental observations in the aspects of terminal bubble shape, terminal velocity and wake flow pattern. Good agreements are obtained in most flow regimes. In addition, it is found that the initial bubble shape may have significant effects on final appearance of the bubble in the flow regimes with intermediate Reynolds and Bond numbers around 200.

The rest of the paper is arranged as follows. Details of the governing equations, non-dimensional parameters and the numerical method are described in Section 2. The numerical simulation results are presented and compared with available experimental data in Section 3. Further discussions on the mechanism of rising bubble’s deformation in viscous liquid under the effects of Reynolds and Bond numbers, initial bubble shape, density and viscosity ratios, are also presented in the later part of Section 3. Finally, the findings and conclusions drawn from this study are summarised in Section 4.

2. Mathematical formulation and numerical method

2.1. Governing equations

For a multi-fluid system if the two fluids can be considered as incompressible, the mass and stress balances on the interface between two fluids may be described as follows [24,5]. Firstly, the normal velocity in each fluid phase on the interface should be continuous, and can be expressed as

$$[\mathbf{u}] \cdot \mathbf{n} = 0, \tag{1}$$

in which the square bracket represents the jump across the interface, \mathbf{u} is the fluid velocity and \mathbf{n} represents the unit normal vector to the interface. Secondly, a stress balance on the interface may be expressed as

$$[-p + \mu(\nabla\mathbf{u} + \nabla^T\mathbf{u})] \cdot \mathbf{n} = \sigma\kappa\mathbf{n}, \tag{2}$$

$$[\mu(\nabla\mathbf{u} + \nabla^T\mathbf{u})] \cdot \mathbf{t} = 0, \tag{3}$$

where p is the pressure in the fluid domain, σ the surface tension, κ the curvature of the interface, \mathbf{t} the unit tangent vector of the interface, and μ the fluid viscosity.

In this study, we investigate the rising of single bubble in a quiescent liquid. It is normally reasonable to treat the liquid phase as incompressible fluid. With the assumption of an isothermal system and neglecting gas density variation caused by the liquid hydraulic pressure, the gas phase of the bubble can also be treated as incompressible fluid. Hence, the mass conservation equation on the whole domain (both fluid phases and the interface) can be expressed in form of volume flux conservation:

$$\nabla \cdot \mathbf{u} = 0. \tag{4}$$

The Navier–Stokes equation, governing the momentum balance in each fluid phase and on the interface, can be expressed as

$$\frac{\partial(\rho\mathbf{u})}{\partial t} + \nabla \cdot \rho\mathbf{u}\mathbf{u} = -\nabla p + \nabla \cdot [\mu(\nabla\mathbf{u} + \nabla^T\mathbf{u})] + \sigma\kappa\mathbf{n}\delta(\mathbf{x} - \mathbf{x}_f) + (\rho - \rho_1)\mathbf{g}, \tag{5}$$

where, $\delta(\mathbf{x} - \mathbf{x}_f)$ is a delta function that is one at the interface only and zero elsewhere, \mathbf{g} the gravitational acceleration. And subscript f refers the front or interface, ρ the density of fluid, and ρ_1 the density of liquid phase.

We introduce the following dimensionless characteristic variables:

$$x^* = \frac{x}{D}; \quad u^* = \frac{u}{(gD)^{1/2}}; \quad \tau^* = \frac{t}{D^{1/2}g^{-1/2}}; \quad \rho^* = \frac{\rho}{\rho_l}; \quad p^* = \frac{p}{\rho_l g D}; \quad \mu^* = \frac{\mu}{\mu_l}; \quad \kappa^* = \frac{\kappa}{D^{-1}}.$$

where D is the effective diameter of a bubble, which is defined as $D = (6V_b/\pi)^{1/3}$, and V_b is the bubble volume. The subscripts l and b stand for the liquid and gas bubble phases, respectively. So, the non-dimensionalised Navier–Stokes equation may be re-expressed as

$$\frac{\partial(\rho\mathbf{u})}{\partial t} + \nabla \cdot \rho\mathbf{u}\mathbf{u} = -\nabla p + \frac{1}{Re} \nabla \cdot [\mu(\nabla\mathbf{u} + \nabla^T\mathbf{u})] + \frac{1}{Bo} \kappa \mathbf{n} \delta(\mathbf{x} - \mathbf{x}_f) + (\rho - 1)\mathbf{g}, \quad (6)$$

in which the superscript * is omitted for convenience. The non-dimensional Reynolds number and Bond number (also known as Eotvos number) for the simulations in this paper are defined as following:

$$Re^* = \frac{\rho_l g^{1/2} D^{3/2}}{\mu_l}; \quad Bo^* = \frac{\rho_l g D^2}{\sigma}.$$

Based on the above formulation, the problem of a bubble rise in liquid could be characterised by four non-dimensional parameters, namely, the ratios of density (ρ_l/ρ_b) and viscosity (μ_l/μ_b) of two fluids, Reynolds number and Bond number. In literature, another dimensionless parameter called Morton number is also used to represent the fluid property [1,15]:

$$M = \frac{g\mu_l^4}{\rho_l\sigma^3} = \frac{Bo^3}{Re^4}.$$

Most experimental results on bubble rising in liquid are presented using the Reynolds number (Re) that was defined using the bubble terminal rising velocity (U_∞) measured:

$$Re = \frac{\rho_l D U_\infty}{\mu_l}.$$

2.2. Treatment of the discontinuities across the front

To solve the Navier–Stokes equations over a fixed grid, the fluid properties (density and viscosity) distribution in the whole solution domain are required. Although the density and viscosity of each fluid is constant as the fluid is assumed to be incompressible, the abrupt jump across the interface of multi-fluid system may lead to either excessive numerical diffusion or numerical instability. The novelty of the front tracking method proposed by Tryggvason et al. [27] is that the interface is considered to have a finite thickness of the same order of the mesh size instead of zero thickness. In the transition zone near the interface, the fluid properties change smoothly and continuously from the value on one side of the interface to the value on the other side. The artificial thickness of the interface depends on the grid size, and is kept constant during the computation. Hence, this method does not have numerical diffusion across the interface. The field distributions $b(\mathbf{x}, t)$ of material properties over the whole solution domain may be reconstructed using an indicator function $I(\mathbf{x}, t)$, which has the value of one in the bubble gas phase and zero in the liquid phase at a given time t :

$$b(\mathbf{x}, t) = b_l + (b_b - b_l) \cdot I(\mathbf{x}, t), \quad (7)$$

in which b stands for either fluid density or viscosity. The indicator function can be written in the form of an integral over the whole domain $\Omega(t)$ with the interface $\Gamma(t)$:

$$I(\mathbf{x}, t) = \int_{\Omega(t)} \delta(\mathbf{x} - \mathbf{x}') d\mathbf{v}', \quad (8)$$

where $\delta(\mathbf{x} - \mathbf{x}')$ is a delta function that has a value of one where $\mathbf{x}' = \mathbf{x}$ and zero every where else. Taking the gradient of the indicator function and transforming the volume integral into an integral over interface yields:

$$\nabla I = \int_{\Gamma(t)} \mathbf{n} \delta(\mathbf{x} - \mathbf{x}') ds, \quad (9)$$

where \mathbf{n} is the unit normal vector on the interface. Taking the divergence of Eq. (9) leads to [27]:

$$\nabla^2 I = \nabla \cdot \int_{\Gamma(t)} \mathbf{n} \delta(\mathbf{x} - \mathbf{x}') ds. \tag{10}$$

Thus, by solving the above Poisson equation in which the right hand side is a function of the known interface position at time t , the indicator function $I(x, t)$ can be reconstructed. Once the indicator function is calculated, the fluid property distribution field can be calculated according to Eq. (7).

A distribution function $D(\mathbf{x})$ is used to approximate the delta function, and it defines the fraction of the interface quantity (such as density and viscosity difference of two phases, and surface tension) distributed to nearby grid point across the artificial thickness of the front. Thus, the sharp jump of the indicator function on the interface is spread among the nearby grids. This generates a gradient field ($\mathbf{G} = \nabla I$), which is none-zero within the finite thickness interface, but otherwise zero everywhere else. The discretized form of the gradient function \mathbf{G} is given as follows [27]:

$$\mathbf{G}(\mathbf{x}) = \sum_f D(\mathbf{x} - \mathbf{x}_f) \mathbf{n}_f \Delta s_f, \tag{11}$$

where \mathbf{n}_f is the unit normal vector at an interface element with an area of Δs_f whose centroid is \mathbf{x}_f . In this study the following distribution function by Peskin [20,21] is used for a two-dimensional grid system:

$$D(\mathbf{x} - \mathbf{x}_f) = \begin{cases} (4h)^{-2} \prod_{i=1}^2 (1 + \cos(\frac{\pi}{2h} |\mathbf{x} - \mathbf{x}_f|)), & \text{if } |\mathbf{x} - \mathbf{x}_f| < 2h \\ 0, & \text{otherwise.} \end{cases} \tag{12}$$

where h is the grid size.

Using the same approach, the surface tension on the front can also be easily distributed to the fixed grid as [27]:

$$F_{st}(\mathbf{x}) = \sum_f D(\mathbf{x} - \mathbf{x}_f) \sigma k \mathbf{n}_f. \tag{13}$$

2.3. Numerical method

A projection method was used to solve the Navier–Stokes equations in the previous works of Tryggvason et al. [27]. They used a fixed, regular, staggered grid and discretized the momentum equations using second-order-centred difference scheme for the spatial variables and explicit second-order time integration. In their method, the front is advected first, and followed by density update. Once the density is updated, the velocity can be computed in the following two steps. In the first step of the projection scheme, the effects of pressure are ignored in the momentum equation, and the flow velocity is projected as follows:

$$\frac{\rho^{n+1} \mathbf{u}^* - \rho^n \mathbf{u}^n}{\Delta t} = -\nabla \cdot \rho^n \mathbf{u}^n \mathbf{u}^n + \nabla \cdot \mu (\nabla \mathbf{u}^n + \nabla^T \mathbf{u}^n) + \mathbf{F}_{st}, \tag{14}$$

where Δt is the time step size, the superscript n and $n + 1$ refer to the current and the next time step, respectively.

Then, a correction step is performed to include the pressure gradient:

$$\frac{\rho^{n+1} \mathbf{u}^{n+1} - \rho^{n+1} \mathbf{u}^*}{\Delta t} = -\nabla p. \tag{15}$$

With the incompressible condition ($\nabla \cdot \mathbf{u}^{n+1} = 0$), the pressure can be obtained by solving the following non-separable elliptic Poisson equation:

$$\nabla \frac{1}{\rho^{n+1}} \cdot \nabla p = \frac{1}{\Delta t} \nabla \cdot \mathbf{u}^*. \tag{16}$$

A number of difficulties have been reported in the literature while solving the above pressure equation. For example, a large density ratio may lead to a problem in convergence [27,3].

In order to overcome the difficulties in solving the pressure equation, an alternative approach is implemented in the present work. Similar to that of Tryggvason et al. [27], we also use a fixed, regular, staggered grid, but discretize the momentum equations using finite volume method. As the front is advected explicitly, the fluid property field and surface tension are updated subsequently. Then, the coupling between flow velocity and pressure is updated by solving the momentum equations and continuity equation using SIMPLE scheme [19] instead of projection method. The simulation process is more robust even in case of large density ratio because of the semi-implicit solving approach:

$$\frac{\rho^{n+1}\mathbf{u}^{n+1} - \rho^n\mathbf{u}^n}{\Delta t} + \nabla \cdot \rho^{n+1}\mathbf{u}^{n+1}\mathbf{u}^{n+1} = -\nabla p^{n+1} + \nabla \cdot \mu(\nabla\mathbf{u}^{n+1} + \nabla^T\mathbf{u}^{n+1}) + \mathbf{F}_{st}^{n+1}. \quad (17)$$

Similar to the conventional approach, the above equation can be solved iteratively, together with the continuity equation, using the volume flux conserved SIMPLE algorithm [19]. In a multi-fluid system, due to the density jump over the interface, the mass flux conservation in the control volume crossing the front interface is not valid. Instead, the volume flux conservation is adopted here to modify the SIMPLE algorithm. The divergence of velocity field over the whole solution domain will be kept at zero, as long as both liquid and gas can be reasonably treated as incompressible fluids. Based on this assumption, SIMPLE algorithm is used to calculate the correction value of pressure and velocity after solving the momentum equation as follows.

In discretized form, the momentum equation can be expressed as the following:

$$a_p\mathbf{U}_p^* = \sum a_{n,p}\mathbf{U}_{n,p}^* + S_p - B\nabla P_p^*, \quad (18)$$

in which n indicates the neighbouring point surrounding the centre point p , and the coefficient $a_{n,p}$ involves the flow properties of convection, diffusion and geometrical property of the control volume. S_p refers the source term and B the coefficient for the pressure gradient term. Details about these coefficients can be obtained in the work of Patankar [19].

Improved pressure field (P_p^{**}) and velocity field (\mathbf{U}_p^{**}) can be obtained by adding the correction terms (\mathbf{U}'_p, P'_p) to the values used in Eq. (18) based on calculation of \mathbf{U}_p^* or assumption of P_p^* :

$$\mathbf{U}_p^{**} = \mathbf{U}_p^* + \mathbf{U}'_p; \quad P_p^{**} = P_p^* + P'_p. \quad (19)$$

Substituting the above equation into Eq. (18), we have the relationship about correction velocity (\mathbf{U}'_p) and correction pressure (P'_p) as follows:

$$\mathbf{U}'_p = \sum a_{n,p}\mathbf{U}'_{n,p}/a_p - B/a_p \cdot \nabla P'_p. \quad (20)$$

Applying incompressible fluid condition to the improved velocity field ($\nabla \cdot \mathbf{U}_p^{**} = 0$), the velocity correction (\mathbf{U}') should satisfy the following condition:

$$\nabla \cdot \mathbf{U}' = -\nabla \cdot \mathbf{U}^*. \quad (21)$$

By taking divergence to the both sides of Eq. (20), ignoring the first term (with high order) on the right hand side of Eq. (20) and substituting it into Eq. (21), the pressure correction can be obtained by solving the following equation:

$$\nabla \cdot [(B/a_p)\nabla P'] = \nabla \cdot \mathbf{U}^*. \quad (22)$$

Based on the pressure correction, the velocity correction can also be derived according to Eq. (20). The updated velocity and pressure are then used as the guessed field for the next iteration for solving the momentum Eq. (18). Such iterations will be repeated until the convergence of both momentum and continuity equations. Compared with the projection method, the SIMPLE algorithm avoids directly solving the pressure equation, which enhances the numerical robustness for the cases with large density/viscosity jumps across the two-fluid interface [4].

2.4. Front tracking

After the velocity field is calculated on the fixed background grid, the velocity of the moving front needs to be interpolated from the velocity at the fixed grid to ensure the front moves at the same velocity as the sur-

rounding fluids. In Section 2.3, the distribution function used to spread the fluid property jump to the fixed grids near the interface was discussed. Similarly, this function can also be used to interpolate field variables from the background grid to the front using the following equation:

$$\mathbf{u}_f = \sum D(\mathbf{x}_f - \mathbf{x})\mathbf{u}(\mathbf{x}). \tag{23}$$

Then, the front is advected along the normal direction in a Lagrangian fashion:

$$\mathbf{x}_f^{n+1} - \mathbf{x}_f^n = \Delta t \mathbf{u}_f. \tag{24}$$

After the front is advected to the new position, the mesh size and quality on the front may be deteriorated due to the deformation of the front. For example, some element points may have moved closer resulting in very small elements. On the contrary, some elements may become larger. The element resolution on the interface has a strong effect on the information exchange between the front and the fixed background grids that in turn affects the accuracy of the simulation results. Hence, front mesh adaptation has to be performed to improve the front mesh quality, but the conservation of bubble volume may be scarified due to the mesh refining and coarsening. To conserve the bubble volume, the front position is corrected by the following equation:

$$\mathbf{x}_f - \mathbf{x}_f^* = (V - V^*)/S^* \cdot \mathbf{n}^*, \tag{25}$$

where $\mathbf{x}_f, \mathbf{x}_f^*$ are the final corrected front position and the current front position respectively. V is the theoretical/initial bubble volume. V^*, S^*, \mathbf{n}^* are the bubble volume, surface area and front outward unit normal vector for the current bubble, respectively.

In the present work, an axisymmetric problem is studied. The bubble front is marked by a set of connected line elements. The element adaptation is based on the upper and lower limits of the element length. One background grid cell normally contains 2–4 front line elements. Similarly, the topology change of the front should also be examined by modifying the element connectivity.

2.5. Solution procedure

With appropriate initial conditions for the fluid flow and interface shape, the solution algorithm proceeds iteratively through the following steps:

- (1) Using the fluid velocity field (\mathbf{u}^n) and the interface position (\mathbf{x}_f^n), the moving velocity of the front marker points (\mathbf{u}_f^n) is computed using Eq. (23).
- (2) Using the estimated normal interface velocity, the front is advected to the new position (\mathbf{x}_f^{n+1}). Subsequently, the elements, representing the front, are examined for adaptation, topology change, and are corrected for conserving the volume enclosed inside the front.
- (3) At the new interface positions, the redistribution of the interface property is performed with the reconstructed indicator function $I(\mathbf{x}_f^{n+1})$. Hence, the new fluid property filed such as density (ρ^{n+1}), viscosity (μ^{n+1}), as well as the surface tension (\mathbf{F}_{st}^{n+1}), are obtained.
- (4) With appropriate wall boundary conditions, the momentum equation and mass continuity equation can be solved implicitly using the modified SIMPLE algorithm. This leads to update fluid velocity (\mathbf{u}^{n+1}) and pressure (p^{n+1}).
- (5) Repeat the solution steps from (1) to (4) for the next time step calculation.

3. Results and discussion

3.1. Experimental observations and modelling strategy

Previous experimental studies on the rising and deforming of single bubble in quiescent liquid have been reported in the literature [5,1,22]. The bubble shapes vary greatly in different flow regimes as a function of the non-dimensional parameters such as Bond number, Reynolds number and Morton number. The terminal

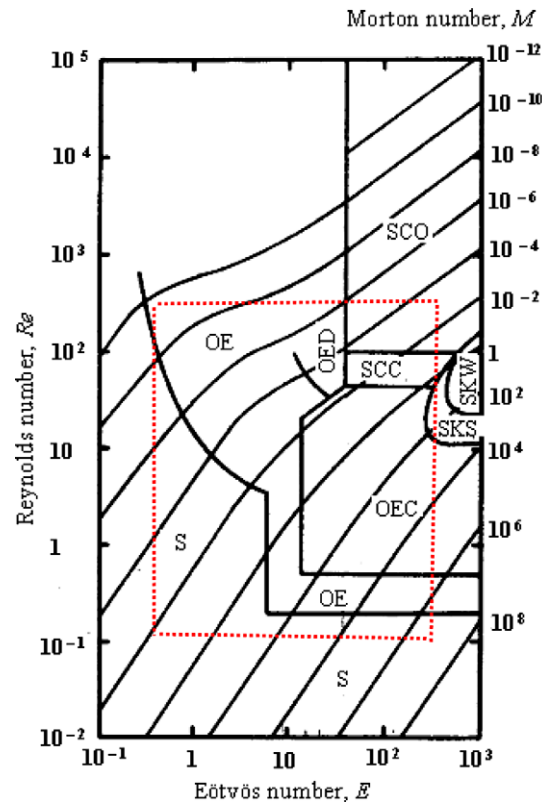


Fig. 1. The regime map of experimental observed rising bubble shape in liquids [1]: S, Spherical; OE, oblate ellipsoid; OED, oblate ellipsoidal (disk-like and wobbling); OEC, Oblate ellipsoidal cap; SCC, Spherical cap with closed, steady wake; SCO, spherical cap with open, unsteady wake; SKS, skirted with smooth, steady skirt; SKW, skirted with wavy, unsteady skirt.

shapes of single rising bubble under a range of Reynolds and Bond numbers were observed and reported in the work by Bhaga and Weber [1] as shown in Fig. 1. Generally, small bubbles, which have low Reynolds or Bond number ($Re < 1$ or $Bo < 1$), rise in a steady fashion and maintain the spherical shape. The shape of larger bubbles, with intermediate Reynolds and Bond numbers ($1 < Re < 100$ and $1 < Bo < 100$), are affected significantly by the flow conditions. Various bubble shapes (oblate ellipsoid, disk-like, oblate ellipsoidal cap, skirt bubble, and spherical-cap) have been found in various flow regimes by the experimental investigations. In spite of the difference in shapes, the bubbles rise steadily in the liquid along a straight path. With further increase of the Reynolds number ($100 < Re < 500$), the bubble shape may become toroidal in the high Bond number ($100 < Bo < 500$) regime; spherical-cap in intermediate Bond number regime ($30 < Bo < 100$) and oblate ellipsoid in the low Bond number regime ($1 < Bo < 30$). As the bubble size increases further, turbulent wake develops behind the bubble that leads to unsteady bubble motion. The bubble may rise in a wobbly path, oscillate about a mean shape and even break up or coalesce. In general, the rising bubbles have axisymmetric shapes when the Reynolds and Bond numbers are not too higher ($Re < 200$, $Bo < 200$) within the range indicated by the dot lines in Fig. 1.

Based on the experimental observations, the single bubble rising in quiescent liquid could be simulated using the front tracking method in an axisymmetric co-ordinate system within certain flow regimes that will produce axisymmetric bubbles. The simulation domain is illustrated in Fig. 2. The solution domain size in the radial direction should be large enough so that the boundary effects on bubble rising can be ignored in the simulation, and the bubble rising can be reasonably assumed as in an infinite quiescent liquid. The effect of solution domain size in the radial direction on the final bubble position and shape is shown in Fig. 3 under the simulation conditions of $Bo^* = 116$, $Re^* = 13.95$, $\rho_l/\rho_b = 1000$ and $\mu_l/\mu_b = 100$. It is clearly shown that the boundary effect is negligible when the radial size of the solution domain is about four times of the bubble

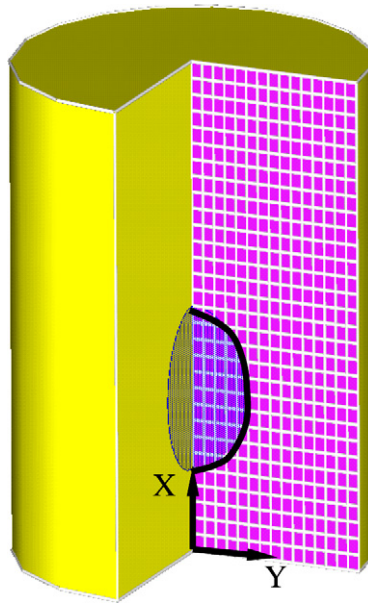


Fig. 2. The schematic diagram of the solution domain for the numerical simulation.

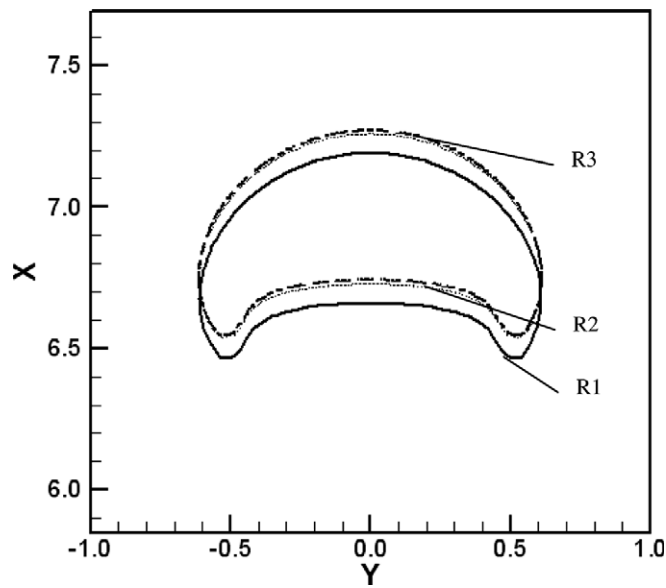


Fig. 3. Effect of solution domain size (with radial radius of $R1 = 3.0$; $R2 = 4.0$; $R3 = 4.8$ times of initial bubble diameter) on the bubble terminal shapes and position at $\tau^* = 10$.

diameter, which is then adopted in this paper. The solution domain size in the axial direction is about twelve times of the bubble diameter. The ideal spherical bubble is located initially on the symmetric axis at two bubble diameters above the bottom. Both liquid and bubble are assumed to be stationary at the initial state.

In this simulation, a uniform fine background mesh was adopted to solve the Navier–Stokes equation. The mesh sensitivity analysis was performed by simulating the bubble rising the under same condition ($Bo^* = 116$, $Re^* = 13.95$, $\rho_l/\rho_b = 1000$ and $\mu_l/\mu_b = 100$) using different sized background mesh. Five different mesh sizes of

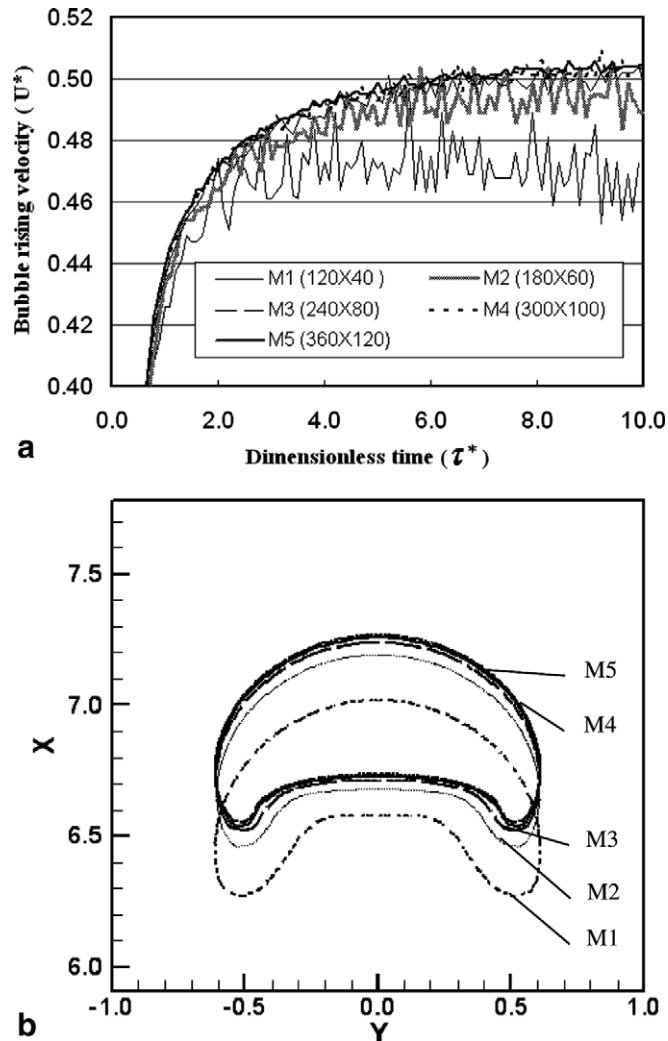


Fig. 4. Effect of mesh sizes on the simulation results (a) bubble rising velocity; (b) the bubble terminal shape and position at $\tau^* = 10$.

M1 (120×40), M2 (180×60), M3 (240×80), M4 (300×100) and (360×120) were applied for the simulations. The effects of mesh size on predicted bubble rising velocity and terminal bubble shape are shown in Fig. 4. When the background mesh is coarse, about ten grids across the bubble (M1), although the initial bubble rising velocity is well predicted with similar accuracy as those with the finer meshes (M4, M5), there are significant fluctuations in bubble rising velocity prediction when it is approaching the steady state, and the mean value is also under predicted. When the mesh is finer (M4 and M5), the predicted bubble rising velocity is more stable. The fluctuation is so smaller compared to the mean value, and hence it is negligible. The predicted bubble rising velocity and bubble will not have significant changes when the mesh finer than M4. Hence, the simulation results reported in this paper is based on background mesh M4, and the bubble is meshed with about twenty-five grids.

Since the mesh for the bubble front is advected explicitly, and is adapted when distorted, the bubble volume inside the front mesh cannot be guaranteed. In addition, the interpolation algorithm to get the moving speed of the interface and numerical truncation error from the fluid property discontinuity across the interface may also lead to the unphysical variation of bubble volume from its physical value in the simulations. Hence, a volume correction scheme is adopted in the paper to ensure that the bubble volume will conserve during the simulation. Under the simulation conditions of $Bo^* = 116$, $Re^* = 13.95$, $\rho_l/\rho_b = 1000$ and $\mu_l/\mu_b = 100$, it

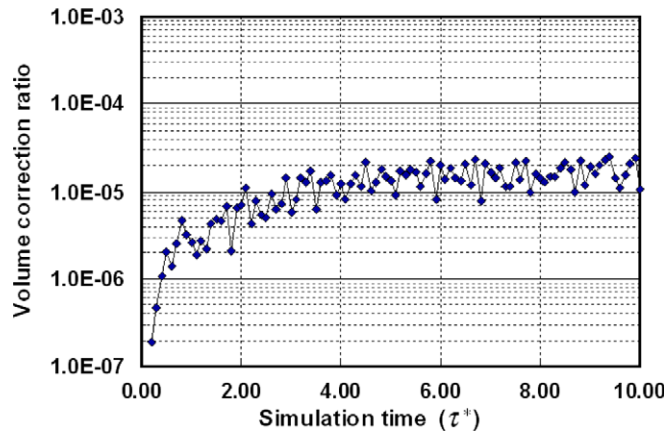


Fig. 5a. Variation of volume correction ration with simulation time.

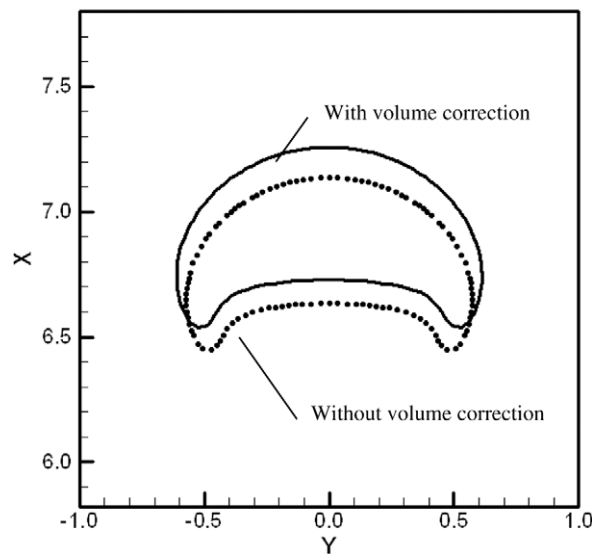


Fig. 5b. Effect of volume correction on the bubble terminal shape and position at $\tau^* = 10$.

can be seen from Fig. 5a that the bubble volume correction ratio is about $2.0\text{E}-5$ at each simulation step. Moreover, this unphysical volume change, although small in each time step, may accumulate during the long simulation. The longer the simulation performs, the larger the error will be accumulated. And, it will affect the final simulation accuracy. The effects of volume correction scheme on the simulation results are illustrated in Fig. 5b by comparing the simulation predicted final bubble positions and shapes with and without volume correction. In case of no volume correction, the bubble volume shrinks about 12% after 5000 time steps simulation compared with the initial value. The predicted bubble rising speed without volume correction is also smaller than that with volume correction. The effects of volume correction on the final simulation results may have the same level of importance as those of the background mesh and domain size as shown in Figs. 3 and 4. Although the volume correction method proposed here is not derived directly from the principles of flow physics, it is a simple and easy way to correct the primary results obtained from front tracking method for complying with the physical observation at each time step, and avoiding the error accumulation during the long simulation of transient problem. The simulation results after adopting the volume correction also have better agreement with the experimental data as discussed in Section 3.2.














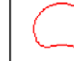

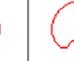













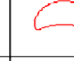








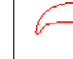






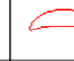



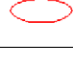
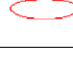
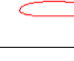
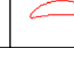
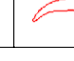
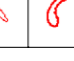
Parameters		Bo*							
		0.5	1	5	10	20	50	100	200
Re*	1								
	5								
	10								
	20								
	50								
	100								
	200								

Fig. 6. The predicted bubble shapes as a function of Reynolds and Bond numbers. The ratios of density and viscosity are set to be $\rho_l/\rho_b = 1000$ and $\mu_l/\mu_b = 100$, respectively.

3.2. Bubble shape and rising velocity

The predicted bubble shapes in a wide range of Reynolds and Bond numbers are summarised in Fig. 6. In the regimes of either low Reynolds or Bond numbers ($Re^* < 1$ or $Bo^* < 1$), the bubbles remain spherical while they are rising in the liquid. With a slight increase in Reynolds number ($Re^* = 5$), the bubble shape still remains spherical for low Bond number, where surface tension is higher. On the other end of high Bond numbers, the bubble bottom becomes flat or slightly dimpled. With the further increases in either Reynolds number ($5 < Re^* < 20$) or Bond number ($0.5 < Bo^* < 20$), bubbles of elliptic/oblate ellipsoid shapes are observed. With further increase in Reynolds number ($50 < Re^* < 100$) and Bond number ($20 < Bo^* < 100$), the bubble shapes range from highly deformed elliptical-cap at lower Reynolds number regime to the spherical-cap bubble at higher Reynolds numbers ($Re^* > 100$). As the bond number increases further ($100 < Bo^* < 200$), skirt bubbles are formed at higher Reynolds numbers ($50 < Re^* < 200$). When the Bond number is increased to the range of $100 < Bo^* < 200$ and $100 < Re^* < 200$, toroidal bubbles are observed. From the simulation results presented here, it can be concluded the current modelling method is robust enough to reasonably predict the various bubble shapes under wider flow regimes.

Besides, detail comparison of the bubble shapes, terminal velocity and wake flow pattern is also necessary to quantitatively understand the accuracy of the predictions. Figs. 7 and 8 compare the terminal bubble shapes obtained from experiments [1] and simulations under a number of experimental test conditions, and Fig. 9 compares the bubble wake flow patterns. The simulation results about predicted bubble shapes shown in Fig. 6 show that the bubble base is dimpled or indented at the intermediate Reynolds number ($5 < Re^* < 100$) and relatively high Bond number ($20 < Bo^* < 50$). The indentation is also clearly visible in bubble photographs shown in cases from B1 to B4, where the upper face the indentation may be seen near the axis of bubbles. At the rim of bubble, the different refractive indices of the gas and the liquid prevent us from seeing how the indentation joins the outer surface of the bubble. If taken this effect into consideration, the simulation predicted terminal bubble shapes agree well with experimental observation [1] for most study cases. In the experiments, the visual observation at lower part of bubbles indicate a rounded lower edge for lower Reynolds numbers, and the edge becomes sharper as Reynolds number increases. The simulation results also clearly show this trend as illustrated in Figs. 7 and 8.





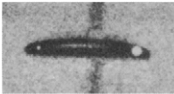

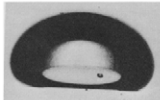

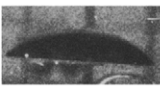







Test Case	Experiments		Simulations	
	Test condition	Observed bubble terminal shape	Predicted bubble Terminal Shape	Modelling conditions
A1	E=8.67 M=711 Re=0.078			Bo*=8.67 Re*=0.979 U*= 0.069
A2	E=17.7 M=711 Re=0.232			Bo*=17.7 Re*=1.671 U*=0.116
A3	E=32.2 M=8.2×10 ⁻⁴ Re=55.3			Bo*=32.2 Re*=79.88 U*=0.663
A4	E=243 M=266 Re=7.77			Bo*=243 Re*=15.24 U*=0.551
A5	E=115 M=4.63×10 ⁻³ Re=94.0			Bo*=115 Re*=134.6 U*=0.659
A6	E=237 M=8.2×10 ⁻⁴ Re=259			Bo*= 237 Re*=357 U*= Unstable
A7	E=339 M=43.1 Re=18.3			Bo*=339 Re*=30.83 U*=0.581
A8	E=641 M=43.1 Re=30.3			Bo*=641 Re*=49.72 U*=6.02×E-1

Fig. 7. Comparison of terminal bubble shapes observed in experiments [1] and predicted in simulation under difference conditions (A1–A8) of various Reynolds, Morton and Bond numbers.

However, the simulation predicted bubble shapes for the study case A6 and B8 are totally different from those observed in experiments [1]. In the experiments a spherical cap bubble with open wake is observed, instead of a toroidal bubble as predicted by simulations. This difference is believed to be caused by the assumption of initial bubble shape as sphere in the simulation. In the following section, we will present more detail discussion on the effects of initial bubble shape on the terminal bubble shape evolution.

The existence of a closed toroidal wake has been observed in experiments by Bhaga and Weber [1] through the flow visualisation using H₂ tracers. The wake flow circulation patterns predicted by the simulation agree well with the observations in experiments as shown in Fig. 9. The wake circulation within the bubble base indentation is clearly shown in the case W3 by the photograph, where the trace track disappears behind the rim of the bubble. The similar wake circulation pattern is revealed in the simulation. In fact, the simulations show that a secondary wake circulation occurs just behind the bubble rim. This may be the reason why the bubble images for the test case W1, W2 and W3 have shown some bright spots at the lower outside of bubble rim. This secondary circulation in the skirt bubble wake becomes much obvious in the simulation case W8. The



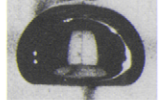







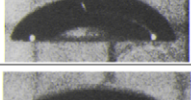

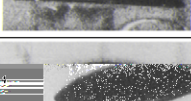
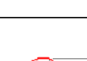
Test Case	Experiments		Simulations	
	Test conditions	Observed terminal bubble shapes	Predicted terminal bubble shapes	Modelling conditions
B1	E=116 M=848 Re=47			Bo*=116 Re*=6.546 U*=0.354
B2	E=116 M=266 Re=3.57			Bo*=116 Re*=8.748 U*=0.414
B3	E=116 M=41.1 Re=7.16			Bo*=116 Re*=13.95 U*=0.502
B4	E=116 M=5.51 Re=13.3			Bo*=116 Re*=23.06 U*=0.571
B5	E=116 M=1.31 Re=20.4			Bo*=116 Re*=33.02 U*=0.602
B6	E=116 M=0.103 Re=42.2			Bo*=116 Re*=62.36 U*=0.634
B7	E=116 M=4.63×10 ⁻³ Re=94.0			Bo*=116 Re*=135.4 U*=0.660

Fig. 8. Comparison of terminal bubble shapes observed in experiments [1] and predicted in simulation under difference conditions (B1–B8) of various Reynolds and Bond numbers.

image of the skirt bubble wake W8 does show a large bright spot just underneath the bubble. As the bubble size increases (with the Reynolds number increasing), the wake volume increases as well, and the wake seems to be torn away from the bubble itself. In this case, the secondary wake circulation disappears, and the bubble base indentation becomes smaller.

The terminal bubble velocity is another important indicator to quantitatively evaluate the difference between the experimental data and simulation results. Based on the parameters given in the experiments, the characteristic parameters (Re^* , Bo^* , ρ_l/ρ_b , μ_l/μ_b) are derived for the simulations, which predict the terminal bubble rising velocity (U_∞^*). Actually, based on this dimensionless terminal velocity, the dimensional terminal bubble velocity U_∞ can be calculated as $U_\infty^* \cdot gD^{1/2}$, and the dimensional terminal bubble velocity based Reynolds number (Re, c) predicted in simulation can be calculated as $Re, c = Re^* \cdot U_\infty^*$. The comparison of the Reynolds numbers for the experiment and simulation cases is listed in Table 1. The results from simulations agree with those of experiments very well within 10% difference.

Most experiments reported by Bhaga and Weber [1] focus on cases with Bond number higher than 20. On the other hand, the experimental work by Raymond and Rosant [22] focus on the single bubble rising behaviour with lower Bond number less than 20. Hence, the both above experimental results are used here to validate the simulation predictions for a wider Bond number range. Table 2 lists the parameters for various simulations for the experimental test cases by Raymond and Rosant [22]. Figs. 10 and 11 present the

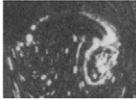







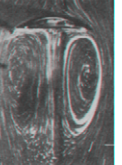
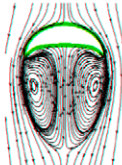
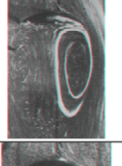
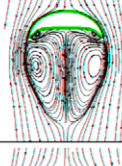
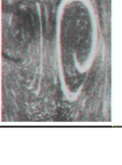
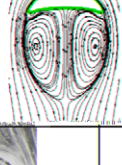
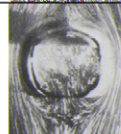
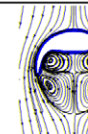
Test Case	Experiments		Simulations	
	Test conditions	Observed terminal bubble shapes	Predicted terminal bubble shapes	Modelling conditions
W1	E=96.2 M=0.962 Re=18.2			Bo*=96.2 Re*=31.0
W2	E=116 M=0.962 Re=22.0			Bo*=116 Re*=35.69
W3	E=95.6 M=1.44×10 ⁻¹ Re=32.4			Bo*=95.6 Re*=49.63
W4	E=151 M=1.44×10 ⁻¹ Re=37.4			Bo*=151 Re*=49.63
W5	E=94.3 M=4.85×10 ⁻³ Re=77.9			Bo*: Re*:
W6	E=114 M=4.85×10 ⁻³ Re=91.6			Bo*: Re*:
W7	E=61.9 M=8.2×10 ⁻⁴ Re=99.5			Bo*: Re*:
W8	Bo*=292 Re*=31.07	E=292 M=26.7 Re=22.1		

Fig. 9. Comparison of terminal bubble wake observed in experiments [1] and predicted in simulation under difference conditions (W1–W8) of various Reynolds, Morton and Bond numbers.

comparisons of bubble terminal velocity and bubble aspect ratios, respectively, between simulations and experiments with different liquid properties and bubble size. Generally, the simulations make good predictions on bubble terminal velocity and shape when the Morton number (M_o) is larger than 1.0×10^{-4} or bubble size is smaller than 5.0 mm. As the bubble becomes larger or the liquid Morton number becomes smaller, the bubble may rise wobbly, and the axisymmetric assumption of bubble shape is not valid. In this situation, a three dimensional model is needed to predict the bubble velocity and shape instead of the axisymmetric model used in this study.

Compared to previous experimental studies by Bhaga and Weber [1] and Raymond and Rosant [22] on the rising bubble shapes in liquid under different flow regimes, the predicted bubble shape and terminal rising

Table 1

Comparison of bubble terminal velocity (in terms of Reynolds number) observed in experiments [1] and predicted in simulations

Test Cases	Experiment		Simulation		$\frac{ Re - Re_c }{Re} \times 100$	
	Re		Re^*	U^*		$Re_c = U^* \times Re^*$
A1	0.078		0.979	0.072	0.0705	9.63
A2	0.232		1.671	0.126	0.211	9.05
A3	55.300		79.880	0.663	52.960	4.23
A4	7.770		15.240	0.551	8.397	8.07
A5	94.000		134.6	0.659	88.701	5.63
A7	18.300		30.830	0.581	17.912	2.12
A8	30.300		49.72	0.602	29.931	1.22
B1	2.470		6.546	0.354	2.317	6.18
B2	3.570		8.748	0.414	3.621	1.45
B3	7.160		13.95	0.502	7.002	2.19
B4	13.300		23.06	0.571	13.167	0.99
B5	20.400		33.02	0.602	19.878	2.56
B6	42.200		62.36	0.634	39.536	6.31
B7	94.000		135.4	0.66	89.364	4.93

Table 2a

The physical properties of fluid used in the series experiments [22] and the simulations in the present study

Series	Experiment				Simulation	
	Viscosity (μ) (Pa S)	Density (ρ) (kg/m^{-3})	Surface tension (σ) (N/m)	Mo	μ^* (μ_b/μ)	ρ^* (ρ_b/ρ)
S1	0.687	1250	0.063	7.0	2.68×10^{-05}	9.42×10^{-4}
S3	0.242	1230	0.063	0.11	7.61×10^{-05}	9.57×10^{-4}
S5	0.0733	1205	0.064	9.0×10^{-4}	2.51×10^{-4}	9.89×10^{-4}
S6	0.0422	1190	0.064	1.0×10^{-4}	4.37×10^{-4}	9.77×10^{-4}

Table 2b

The simulation parameters for the rising of different sized bubbles in the series fluids

Bubble diameter (m)	S1		S3		S5		S6	
	Re^*	Bo^*	Re^*	Bo^*	Re^*	Bo^*	Re^*	Bo^*
0.001	0.180	0.194	0.502	0.191	1.625	0.184	2.788	0.182
0.003	0.935	1.750	2.610	1.722	8.445	1.660	14.491	1.639
0.005	2.012	4.86	5.616	4.783	18.172	4.612	31.181	4.555
0.007	3.334	9.527	9.303	9.375	30.103	9.041	51.652	8.928
0.009	4.860	15.750	13.563	15.498	43.886	14.945		
0.011	6.567	23.527	18.326	23.151	59.299	22.326		

velocity using the present modelling approach are in reasonable agreement. Most of the previous numerical studies on bubble rise in liquids are limited to certain regimes. For example, in the work of [27], the bubble rise was simulated in the regimes of low Reynolds or low Bond numbers. The present work extends its capability to simulate the bubble rise and deformation for a wider flow regime of the realistic “air bubble/water solution” two-fluid flow system.

3.3. Effect of initial bubble shape

Most previous research efforts on simulation [4,25] focused on studying the terminal velocity and shape of bubble rising in quiescent liquid. However, the effect of initial bubble shape on the bubble evolution

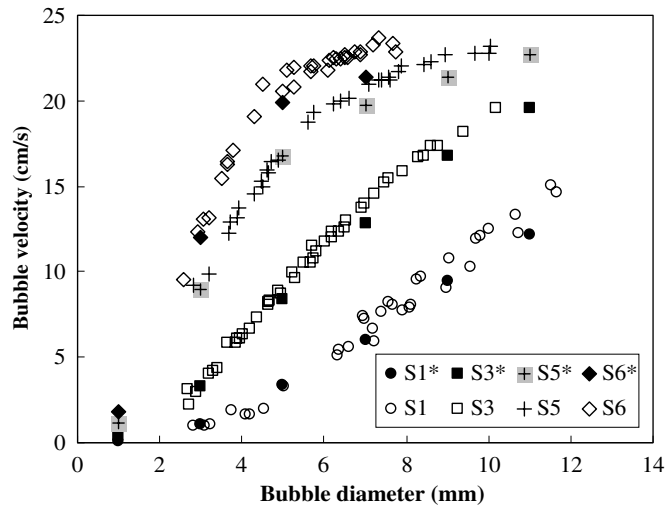


Fig. 10. Comparison of terminal bubble rising velocity predicted by simulations (represented by solid symbols) with experimental observations [22] (represented by hollow symbols).

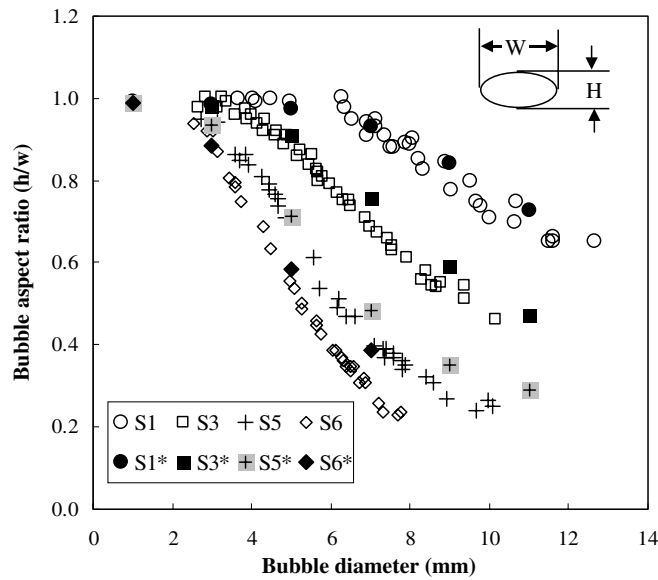


Fig. 11. Comparison of terminal bubble shape aspect ratio predicted by simulations with experimental observations [22].

and terminal velocity is not well studied [17]. Fig. 12 shows the bubble shape evolution history from the different initial bubble shape with different aspect ratios under the flow condition of $Re^* = 13.95$, $Bo^* = 116$, $\rho_l/\rho_b = 1000$ and $\mu_l/\mu_b = 100$ (case B3 in Section 3.2). Under such conditions, the terminal bubbles are quite similar even though the initial bubble shapes are different. From the difference of final bubble positions, it can be concluded that the bubble rising velocity are affected by different initial bubble shape. Fig. 13 depicts the variations of the bubble rising velocity with time. It is observed that the initial bubble with higher aspect ration (H/W) has higher initial rising velocity due to lower flow resistance drag. When the bubble approaches the terminal shape, its rising velocity also reaches its steady terminal value.

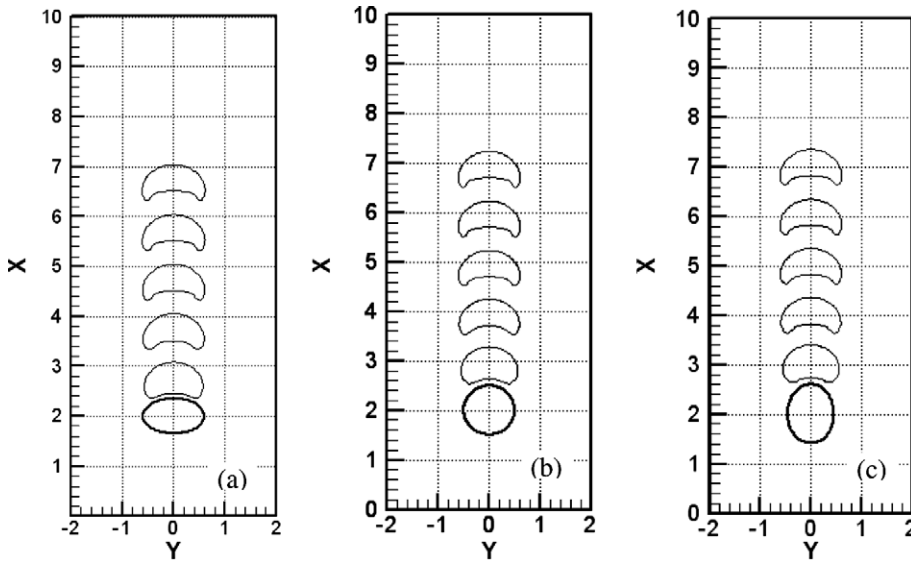


Fig. 12. The evolution of the terminal bubble shape at time interval of $\Delta\tau^* = 1$ under the same conditions of $Bo^* = 116$, $Re^* = 13.95$, $\rho_l/\rho_b = 1000$ and $\mu_l/\mu_b = 100$, but different initial shapes in aspect ratios of (a) $H/W = 0.59$, (b) $H/W = 1.00$ and (c) $H/W = 1.31$.

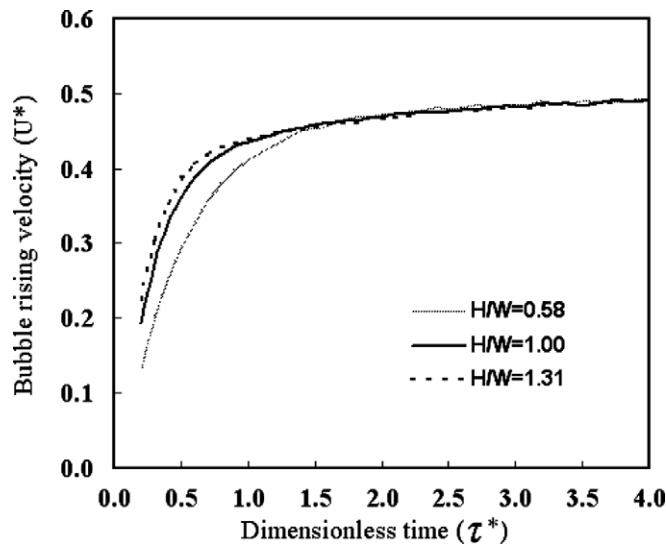


Fig. 13. The predicted bubble rising velocity with time under the same conditions of $Bo^* = 116$, $Re^* = 13.95$, $\rho_l/\rho_b = 1000$ and $\mu_l/\mu_b = 100$, but different initial shapes in aspect ratios of $H/W = 0.59$, $H/W = 1.00$ and $H/W = 1.31$.

Fig. 14 shows the predicted bubble shape evolution history from different initial shapes under the flow conditions of $Re^* = 206.3$, $Bo^* = 116$, $\rho_l/\rho_b = 1000$ and $\mu_l/\mu_b = 100$ (case B8 in Section 3.2). Unlike the case of lower Re^* , the initial bubble shapes have significant effect on the final bubble shape development in this flow regime. The spherical cap bubble is to be formed when the initial bubble shape aspect ratio is lower, and toroidal bubble is expected when the initial bubble shape aspect ratio is higher. The temporal evolution of bubble shape, velocity field, flow speed distribution and pressure field is shown in Figs. 15 and 16, respectively, with initial bubble aspect ratio (H/W) of 0.59 and 1.31. The plots are generated basing on the reference frame located on the top stagnation point of the bubble.

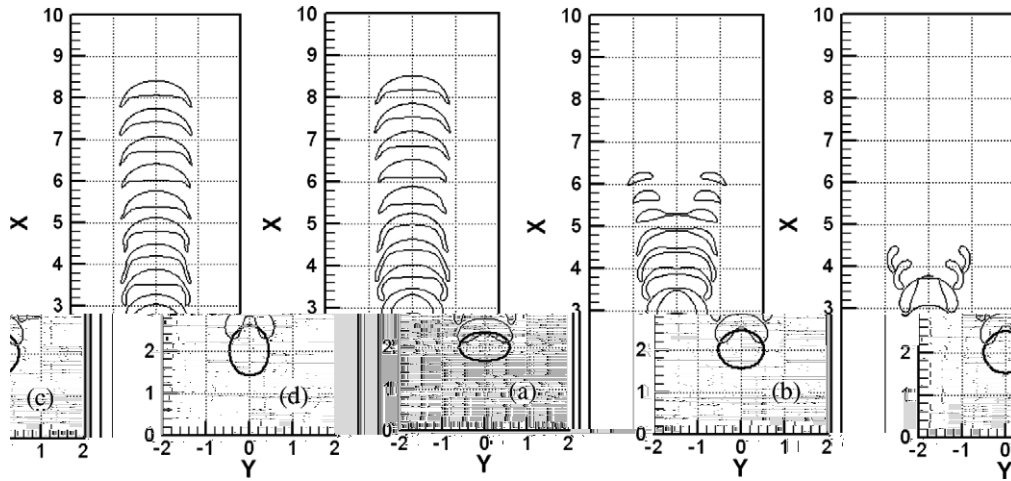


Fig. 14. The evolution of the terminal bubble shape at time interval of $\Delta\tau^* = 1$ under the same conditions of $Bo^* = 116$, $Re^* = 206.3$, $\rho_l/\rho_b = 1000$ and $\mu_l/\mu_b = 100$, but different initial bubble shapes in aspect ratios of (a) $H/W = 0.59$, (b) $H/W = 0.85$, (c) $H/W = 1.00$ and (d) $H/W = 1.31$.

The shape evolution mechanism of rising bubble in a viscous liquid is demonstrated in Figs. 15 and 16. The contour plots of non-dimensional flow velocity distribution are drawn in twenty levels from 0 to 1.5, and the contour plots of non-dimensional pressure field also in twenty levels from -0.5 to 0.5 . When a bubble is merged in the liquid, due to the density difference between bubble and liquid ($\rho_l > \rho_b$), the hydraulic pressure difference across the bubble leads to the buoyancy force acting on bubble that stimulates an upward bubble motion in the viscous liquid (as shown in Figs. 15 and 16 at $\tau^* = 0.5$). The bubble will accelerate as long as the buoyancy force is greater than the resistance drag by the surrounding liquid. As a result, the fluid flow in the liquid is established in the region surrounding the bubble. This leads to a high pressure gradient at the bottom surface of the bubble as shown in Fig. 16 ($\tau^* = 1.0, 1.5$). This high-pressure gradient also induces an upward rising liquid jet underneath the bubble (refer to Fig. 16 ($\tau^* = 1.0$)). The strength of this liquid jet depends upon the difference between the buoyancy force (characterised by the bubble size and density difference between two fluids) and the viscous drag (characterised by bubble shape and fluid viscosity). As the bubble rises further, the upper surface contacting the quiescent liquid receives a relatively steady flow resistance. On the other hand, the strong liquid jet underneath the bubble pushes its bottom surface upward into the bubble (see Fig. 16 ($\tau^* = 1.0$)), which results in the deformation of bubble shape. This bubble deformation then causes a change in the interface curvature and surface tension force. In principle, the surface tension force tends to keep bubble to a spherical shape. A high Reynolds number and high bubble acceleration always indicate a strong liquid jet underneath the bubble. And, a high Bond number represents low surface tension, thus an easily deformable bubble. Eventually, the relative strength between the liquid jet and the surface tension determines whether the lower surface can pierce through the top of the bubble that forms a toroidal bubble as shown in Fig. 16 ($\tau^* = 2.0$), or just approaches the top surface and then recover back to form a spherical cap bubble as shown in Fig. 15 ($\tau^* = 2.0, 2.5$). The toroidal bubble will keep on expanding further in the radial direction (Fig. 16 ($\tau^* = 2.5, 3.0$)). Similar features of the formation of toroidal bubbles developed from spherical bubbles in viscous liquids were also reported in the experimental works of Walters and Davidson [28,29].

The final bubble shape is highly related to the strength of liquid jet formed underneath the bubble, which depends upon the balance of buoyancy force and flow drag resistance. Even though the net buoyancy force is dependant upon the bubble volume, the drag resistance from the viscous liquid has strong dependence upon the bubble shape. When bubble aspect ratio (H/W) is smaller (refer to Fig. 15), the flow resistance on the bubble will be higher, and the bubble will rise at a lower speed forming a weak liquid jet at the bubble bottom. And finally, a spherical cap bubble is formed. In the simulation cases A6 and B8

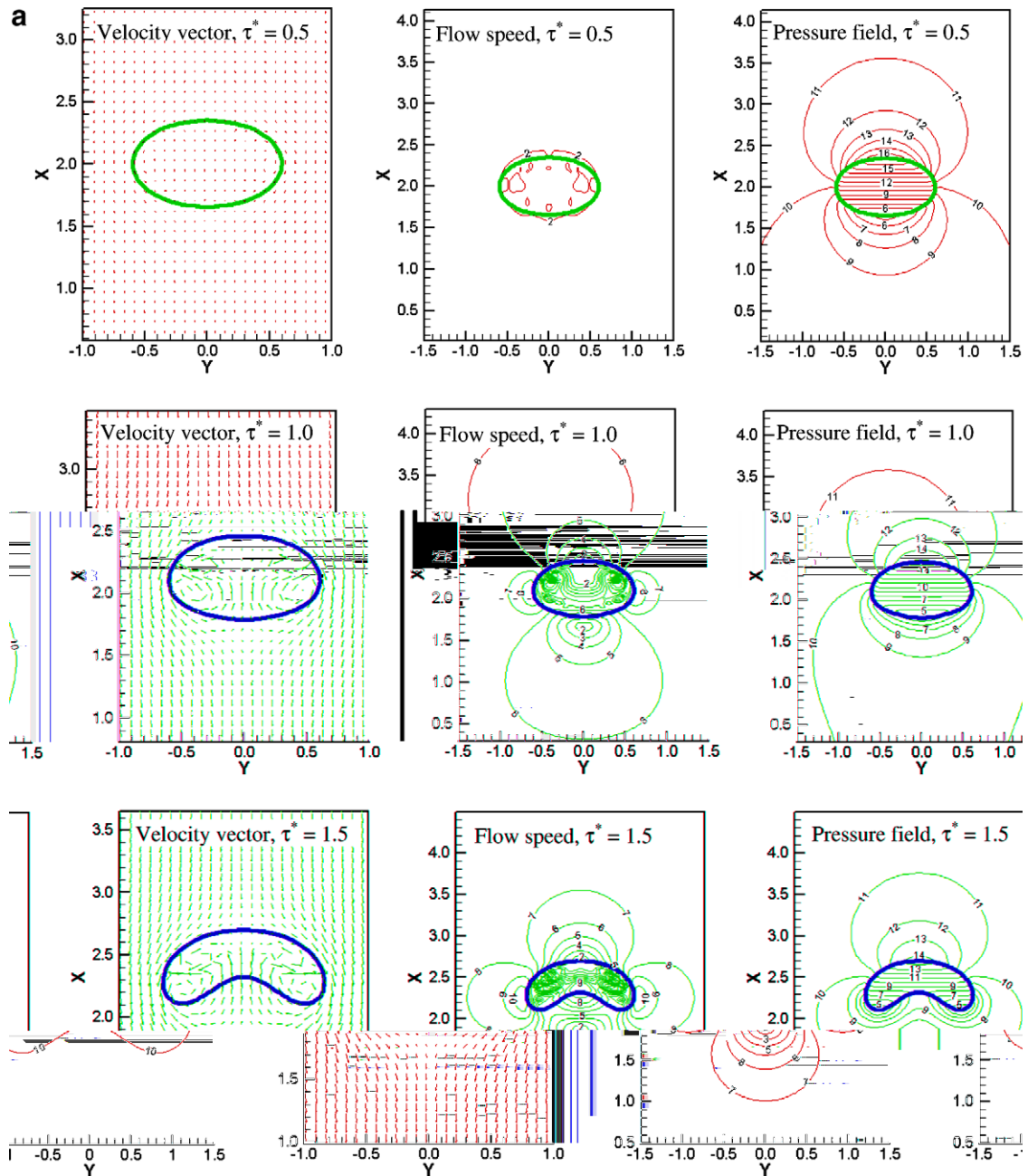


Fig. 15. The temporal evolution of velocity field, and flow speed distribution, and pressure field at interval of $\Delta\tau^* = 1$ under the conditions of $Bo^* = 116$, $Re^* = 206.3$, $\rho_l/\rho_b = 1000$, $\mu_l/\mu_b = 100$ and with initial bubble shapes of $H/W = 0.59$.

reported in Section 3.2, the initial bubble shapes are assumed to be spherical, and toroidal bubbles are predicted. In fact, the spherical cap bubbles were observed in experiments [1]. Through this study, it is understood that the discrepancy between simulations and experimental observations is caused by the assumption of initial bubble shape as spherical in the modelling. In the experiments [1,22], the bubble was first held by a hemi-spherical or cylindrical dumping cup with a relatively large size, and it was then released by turning the cup. When the bubble size is small, it may remain spherical shape due to high

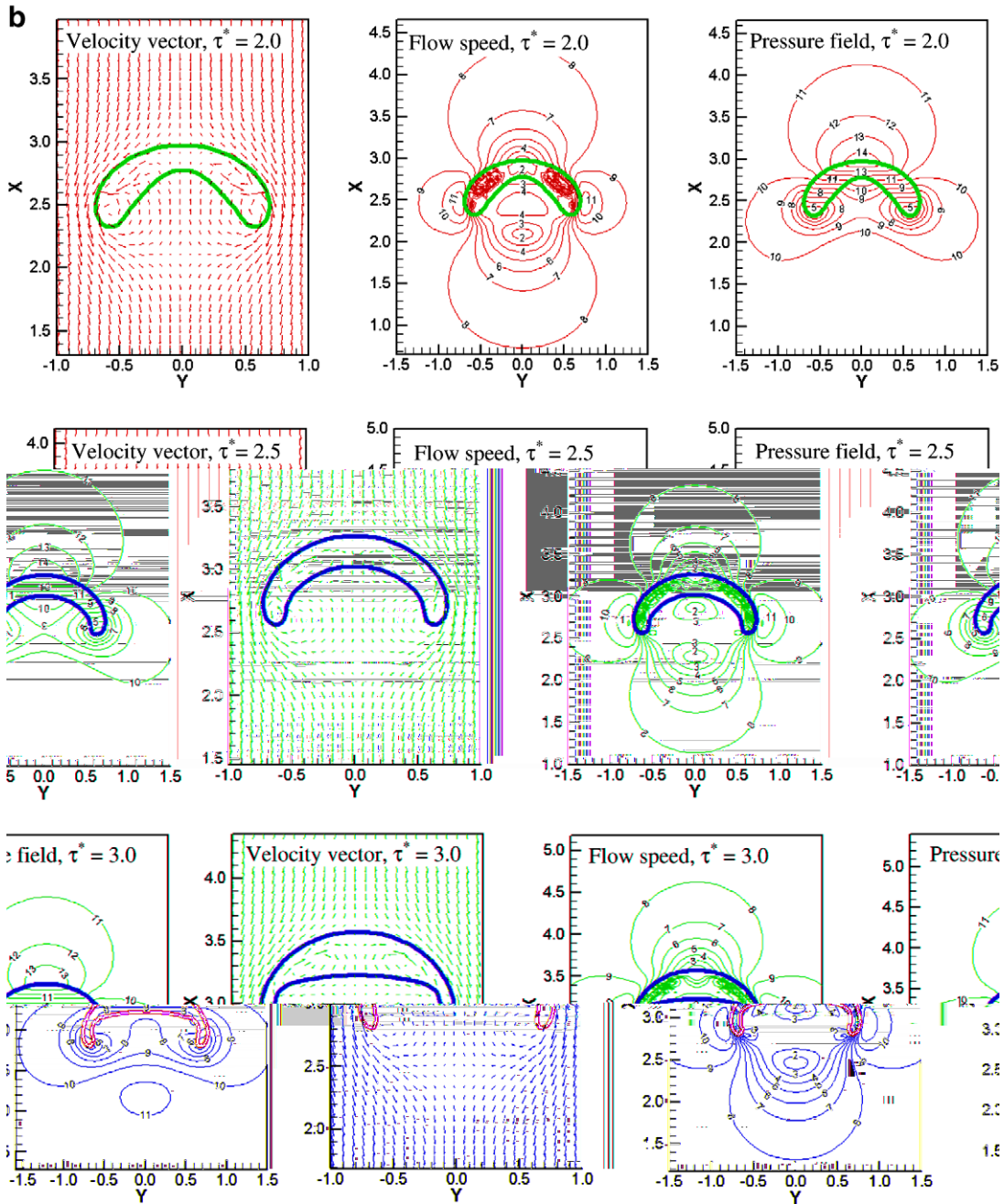


Fig. 15 (continued)

surface tension force caused by high bubble surface curvature, even it is trapped in the dumping cup. However, when the bubble size is large, the bubble will deform to ellipsoidal shape due to stronger buoyancy force and lower surface tension force caused by smaller bubble surface curvature. Hence, the initial bubble will have lower aspect ratio for experimental cases A6 and B8 in Section 3.2. Simulation results shown in Fig. 15 clearly demonstrate that the present model can predict the bubble shape correctly as long as the initial bubble shape assumption agrees with the experimental condition.

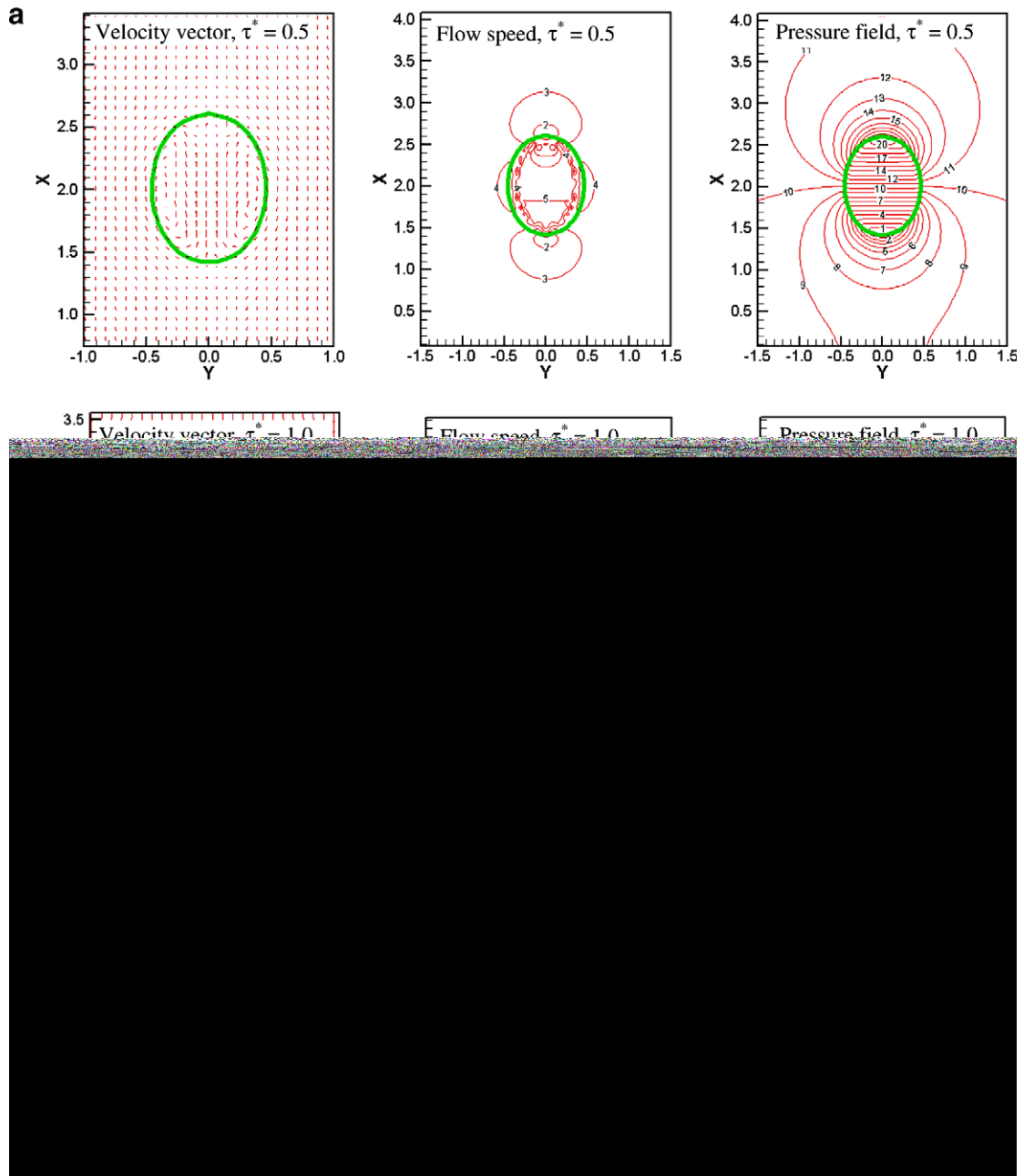


Fig. 16. The temporal evolution of velocity field, and flow speed distribution, and pressure field at interval of $\Delta\tau^* = 1$ under the conditions of $Bo^* = 116$, $Re^* = 206.3$, $\rho_l/\rho_b = 1000$, $\mu_l/\mu_b = 100$ and with initial bubble shapes of $H/W = 1.31$.

3.4. The effect of Reynolds and Bond numbers on bubble rising

As discussed above, the Reynolds number and Bond number affect the bubble shape and the formation of toroidal bubble. Generally, higher Reynolds number would induce larger deformation of bubble-shape in the vertical direction due to the formation of a liquid jet beneath the bubble. On the other hand, the Bond number controls the deformability of the bubble away from a spherical shape. Higher Bond number allows larger deformation. The final bubble shape depends upon the relative strength of the flow forces and the surface ten-

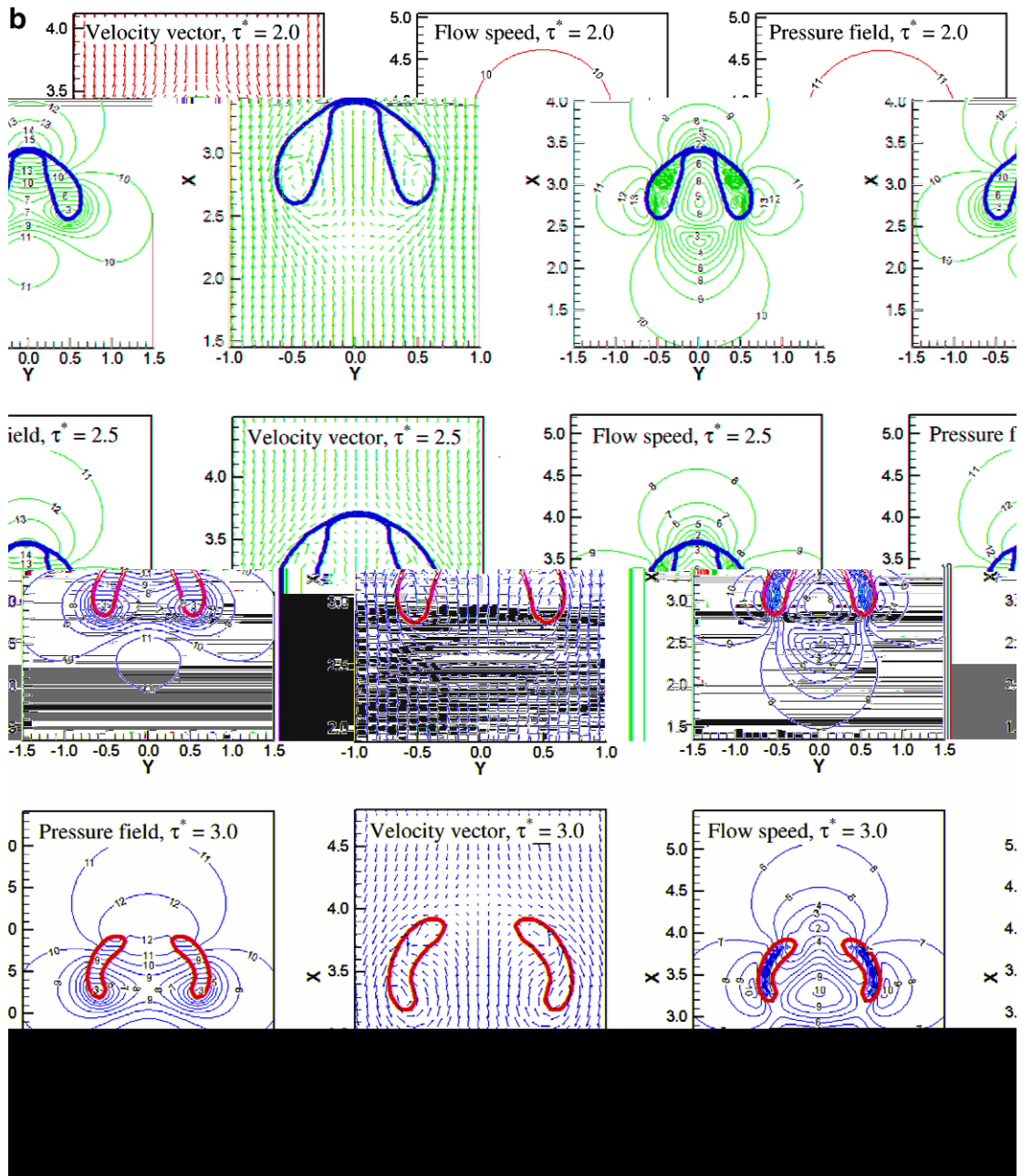


Fig. 16 (continued)

sion force, which are indicated by the Reynolds number and Bond number, respectively. Similar observations have also been reported in Chen et al. [4].

3.5. The effect of density and viscosity ratios on the bubble rising

Fig. 17 shows the predicted bubble position and shape at time $\tau^* = 10$ with different density ratios ρ_1/ρ_b of (a) 2, (b) 5, (c) 20 and (d) 200, while other parameters remain the same ($Re^* = 8.75$, $Bo^* = 116$, $\mu_1/\mu_b = 100$). The variation of bubble rising terminal velocity with density ratios is shown in Fig. 18. It can be seen from Figs. 17 and 18 that density ratio has little effects on final shape and terminal velocity of rising bubble when it is larger than 50.

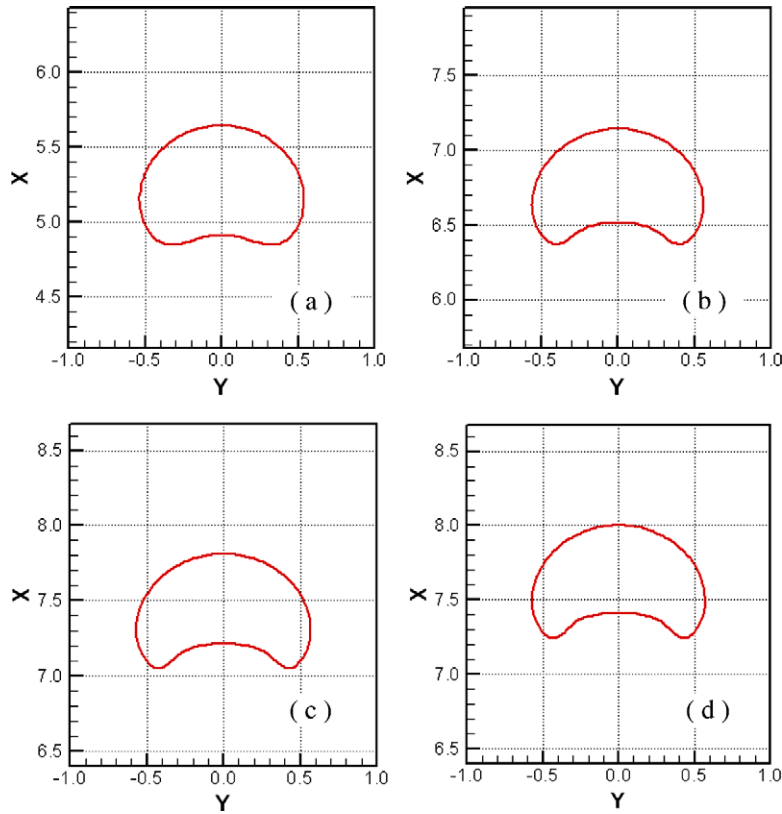


Fig. 17. The predicted terminal bubble shape and position under the conditions of $Bo^* = 116$, $Re^* = 8.75$, $\mu_l/\mu_b = 100$ and initial spherical shape, but different density ratios of (a) $\rho_l/\rho_b = 2$, (b) $\rho_l/\rho_b = 20$ and (c) $\rho_l/\rho_b = 200$.

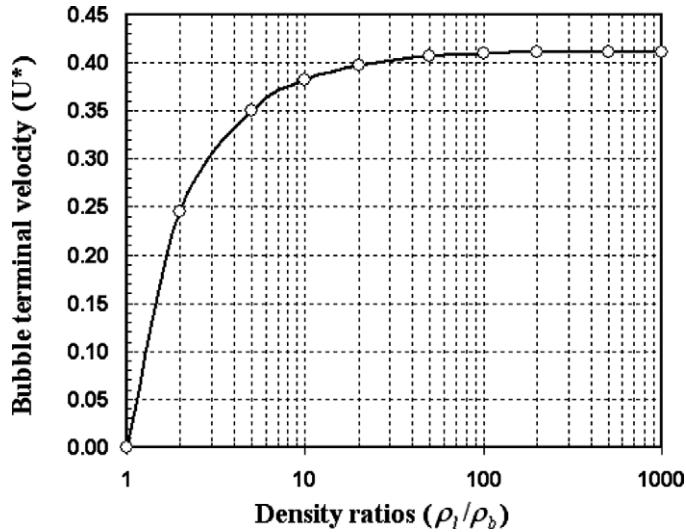


Fig. 18. The predicted terminal bubble velocity varying with density ratios under the conditions of $Bo^* = 116$, $Re^* = 8.75$, $\mu_l/\mu_b = 100$ and spherical initial shape.

A theoretical analysis of Eq. (6) shows that effect of the density ratio is reflected as a factor $(\rho_b/\rho_l - 1)$ in the buoyancy force term. It is obvious that the value of $(\rho_b/\rho_l - 1)$ is significantly affected only at the low density-ratio. The effect of density ratio on bubble rising velocity is more significant than on terminal bubble shape.

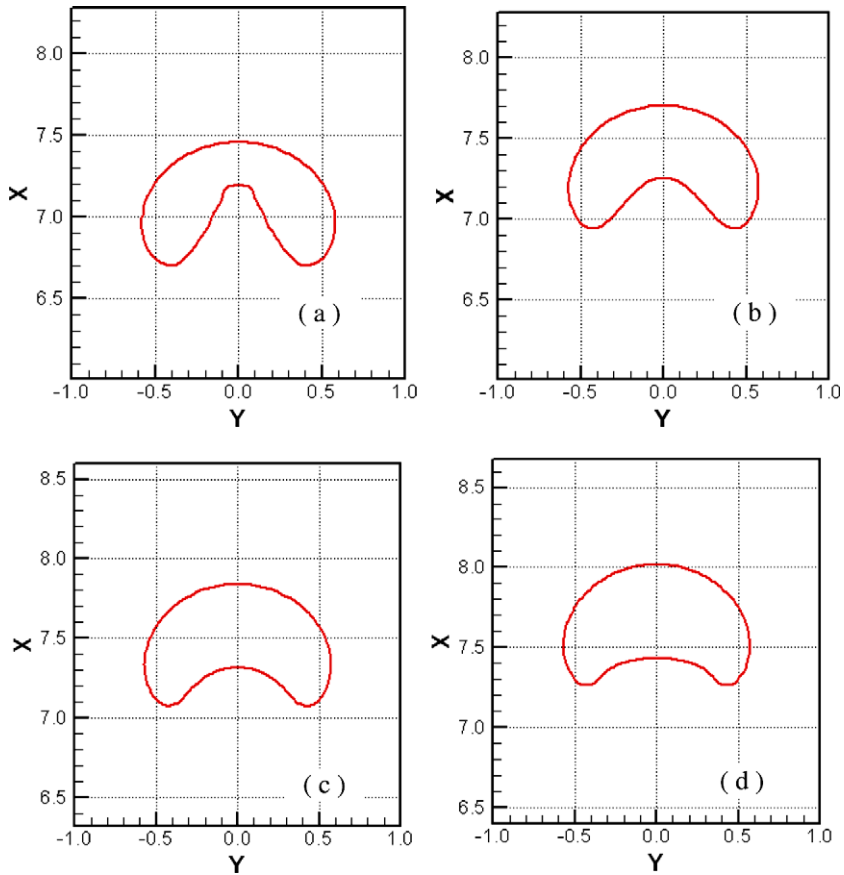


Fig. 19. The predicted terminal bubble shape and position under the conditions of $Bo^* = 116$, $Re^* = 8.75$, $\rho_l/\rho_b = 1000$ and initial spherical shape, but different density ratios of (a) $\mu_l/\mu_b = 2$, (b) $\mu_l/\mu_b = 5$, (c) $\mu_l/\mu_b = 10$ and (d) $\mu_l/\mu_b = 100$.

Fig. 19 shows the predicted bubble shapes at time $\tau^* = 10$ for different viscosity ratios (μ_l/μ_b) of (a) 2, (b) 5, (c) 10 and (d) 100, while other flow parameters remain same ($Re^* = 8.75$, $Bo^* = 116$, $\rho_l/\rho_b = 1000$). Fig. 20 shows the variation of terminal bubble velocity with the viscosity ratio. It is found that the bubble shape

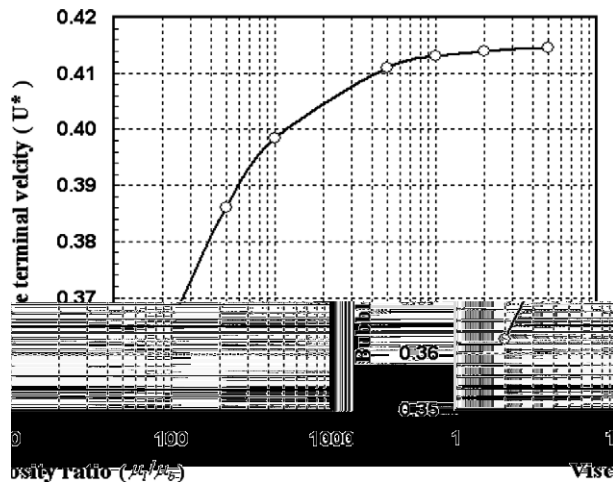


Fig. 20. The predicted terminal bubble velocity varying with viscosity ratios under the conditions of $Bo^* = 116$, $Re^* = 8.75$, $\rho_l/\rho_b = 1000$ and spherical initial shape.

and terminal velocity depend more on the viscosity ratio between bubble and liquid in the low viscosity regime. The effect of viscosity ratio on bubble shape is stronger than on bubble velocity. As shown in Fig. 20, the variation of bubble rising velocity is less than 10% when the viscosity ratio changes from 2 to 500.

4. Conclusions

A front tracking method for modelling two-phase fluid systems has been examined, improved and validated for wider flow regimes. The new algorithm adopts the treatment of the interface with a finite thickness as proposed by Tryggvason et al. The fluid properties (density, viscosity and surface tension) is varied smoothly over the interface, and updated with the interface positions. The interface is advected using the velocity that is interpolated from the velocity field on the fixed background grid. The front mesh size is adapted to match the background mesh size due to its variation in front moving and deforming, and the front mesh position is corrected to conserve the volume enclosed. The velocity field has been solved with the finite volume method over the fixed grid using the volume flux conservation based SIMPLE algorithm. Compared with the projection method, this new algorithm avoids directly solving the pressure equations. It enhances the numerical stability and simulation robustness for large density/viscosity jumps across interface with about thousand times difference. It therefore provides a widely feasible simulation tool for more practical multiphase and interfacial flow applications.

The newly proposed algorithm is applied to simulate the rising of single bubble in a viscous liquid. The bubble shapes and velocity in a wide flow regime are studied as a function of the non-dimensional parameters such as Reynolds number, Bond number, density ratio and viscosity ratio. The comparison of simulations with the available experiments shows satisfactory agreements. In addition, the history of a bubble-rise from the various initial bubble shapes to the terminal shapes is also simulated to understand the mechanism that governs the bubble shape development. The effects of density and viscosity ratios between two fluids on bubble shape development are also analysed.

References

- [1] D. Bhaga, M.E. Weber, Bubbles in viscous liquid: shapes, wakes and velocities, *J. Fluid Mech.* 105 (1981) 61–85.
- [2] L.A. Bozzi, J.Q. Feng, T.C. Scott, A.J. Pearlstein, Steady axisymmetric motion of deformable drops falling or rising through a homoviscous fluid in a tube at intermediate Reynolds number, *J. Fluid Mech.* 336 (1997) 1–32.
- [3] B. Bunner, G. Tryggvason, Dynamics of homogenous bubbly flows. Part 1. Rise velocity and microstructure of the bubbles, *J. Fluid Mech.* 466 (2002) 17–52.
- [4] L. Chen, S.V. Garimella, J.A. Reizes, E. Leonardi, The development of a bubble rising in a viscous liquid, *J. Fluid Mech.* 387 (1999) 61–96.
- [5] R. Clift, J.R. Grace, M.E. Weber, *Bubbles, Drops, and Particles*, Academic Press, 1978.
- [6] B.J. Daly, Numerical study of two fluid Rayleigh–Taylor instability, *Phys. Fluids* 10 (1967) 297–307.
- [7] B.J. Daly, A technique for including surface tension effect in hydrodynamics calculation, *J. Comput. Phys.* 4 (1969) 97–117.
- [8] R.M. Davies, F.I. Taylor, The mechanism of large bubbles rising through extended liquids and through liquids in tubes, *Proc. Royal Soc. Lond. A* 200 (1950) 375–390.
- [9] J. Glimm, O. McBryan, R. Menikoff, D.H. Sharp, Front tracking applied to Rayleigh–Taylor instability, *SIAM J. Sci. Statist. Comput.* 7 (1986) 230–251.
- [10] F.H. Harlow, J.E. Welch, Numerical calculation of time-dependent viscous incompressible flow of fluid with free surface, *Phys. Fluids* 8 (1965) 2182–2189.
- [11] R.A. Hartunian, W.R. Sears, On the instability of small gas bubbles moving uniformly in various liquids, *J. Fluid Mech.* 3 (1957) 27–47.
- [12] C.W. Hirt, B.D. Nichols, Volume of fluid (VOF) method for the dynamics of free boundaries, *J. Comput. Phys.* 39 (1981) 201–225.
- [13] S.I. Kang, G.L. Leal, Numerical solution of axisymmetric, unsteady free-boundary problem at finite Reynolds number. I. Finite-difference scheme and its application to the deformation of a bubble in a uniaxial straining flow, *Phys. Fluids* 30 (1987) 1929–1940.
- [14] M. Koebe, D. Bothe, H.-J. Warnecke, Direct numerical simulation of air bubbles in water/glycerol mixtures: shapes and velocity fields. In: *Proc. FEDSM'03: 4th ASME–JSME Joint Fluids Engineering Conference (FEDSM2003-45154)* (2003). pp. 1–7.
- [15] T. Maxworthy, C. Gnann, M. Kurten, F. Durst, Experiments on the rise of air bubbles in clean viscous liquids, *J. Fluid Mech.* 321 (1996) 421–441.
- [16] D.W. Moore, The rise of a gas bubble in viscous liquid, *J. Fluid Mech.* 6 (1959) 113–130.
- [17] M. Ohta, T. Imura, Y. Yoshida, M. Sussman, A computational study of the effect of initial bubble conditions on the motion of a gas bubble rising in viscous liquids, *Int. J. Multiphase Flow* 31 (2005) 223–237.

- [18] S. Osher, J.A. Sethian, Fronts propagating with curvature dependant speed: algorithm based on Hamilton–Jacobi formulations, *J. Comput. Phys.* 79 (1988) 12–49.
- [19] S.V. Patankar, *Numerical heat transfer and fluid flow*, Hemisphere, 1980.
- [20] C.S. Peskin, Numerical analysis of blood flow in the heart, *J. Comput. Phys.* 25 (1977) 220–252.
- [21] C.S. Peskin, B.F. Printz, Improved volume conservation in the computation of flows with immersed boundaries, *J. Comput. Phys.* 105 (1993) 33–46.
- [22] F. Raymond, J.-M. Rosant, A numerical and experimental study of the terminal velocity and shape of bubbles in viscous liquids, *Chem. Eng. Sci.* 55 (2000) 943–955.
- [23] G. Ryskin, L.G. Leal, Numerical simulation of free-boundary problems in fluid mechanics. Part 2. Buoyancy-driven motion of a gas bubble through a quiescent liquid, *J. Fluid Mech.* 148 (1984) 19–35.
- [24] R. Scardovelli, S. Zaleski, Direct numerical simulation of free-surface and interfacial flow, *Annu. Rev. Fluid Mech.* 31 (1999) 567–603.
- [25] Sint Van Annaland, N.G. Deen, J.A.M. Kuipers, Numerical simulation of gas bubbles behaviour using a three-dimensional volume of fluid method, *Chem. Eng. Sci.* 60 (2005) 2999–3011.
- [26] T.D. Taylor, A. Acrivos, On the deformation and drag of a falling viscous drop at low Reynolds number, *J. Fluid Mech.* 18 (1964) 466–476.
- [27] S.O. Unverdi, G. Tryggvason, A front-tracking method for viscous, incompressible, multi-fluid flows, *J. Comput. Phys.* 100 (1992) 25–37.
- [28] J.K. Walters, J.F. Davidson, The initial motion of a gas bubble formed in an inviscid liquid. Part 1. The two-dimensional bubble, *J. Fluid Mech.* 12 (1962) 408–417.
- [29] J.K. Walters, J.F. Davidson, The initial motion of a gas bubble formed in an inviscid liquid. Part 2. The three dimensional bubble and the toroidal bubble, *J. Fluid Mech.* 17 (1963) 321–336.
- [30] P.P. Wegener, J.Y. Parlange, Spherical-cap bubbles, *Ann. Rev. Fluid Mech.* 5 (1973) 79–100.